

# eRASSt J040515.6–745202, an X-ray burster in the Magellanic Bridge

F. Haberl<sup>1</sup>, G. Vasilopoulos<sup>2</sup>, C. Maitra<sup>1</sup>, F. Valdes<sup>3</sup>, D. Lang<sup>4</sup>, V. Doroshenko<sup>5</sup>, L. Ducci<sup>5</sup>, I. Kreykenbohm<sup>6</sup>, A. Rau<sup>1</sup>, P. Weber<sup>6</sup>, J. Wilms<sup>6</sup>, P. Maggi<sup>2</sup>, C. D. Bailyn<sup>7</sup>, G. K. Jaisawal<sup>8</sup>, P. S. Ray<sup>9</sup>, and H. Treiber<sup>10</sup>

<sup>1</sup> Max-Planck-Institut für extraterrestrische Physik, Gießenbachstraße 1, D-85748 Garching, Germany, e-mail: fwh@mpe.mpg.de

<sup>2</sup> Université de Strasbourg, CNRS, Observatoire astronomique de Strasbourg, UMR 7550, F-67000 Strasbourg, France

<sup>3</sup> NSF's National Optical/Infrared Research Laboratory (NOIRLab), 950 N. Cherry Ave, Tucson, AZ 85732, USA

<sup>4</sup> Perimeter Institute for Theoretical Physics, 31 Caroline Street North, Waterloo, ON N2L 2Y5, Canada

<sup>5</sup> Institut für Astronomie und Astrophysik, Sand 1, D-72076 Tübingen, Germany

<sup>6</sup> Remis Observatory and ECAP, Universität Erlangen-Nürnberg, Sternwartstraße 7, D-96049 Bamberg, Germany

<sup>7</sup> Department of Astronomy, Yale University, PO Box 208101, New Haven, CT 06520-8101, USA

<sup>8</sup> DTU Space, Technical University of Denmark, Elektrovej 327-328, DK-2800 Lyngby, Denmark

<sup>9</sup> U.S. Naval Research Laboratory, Washington, DC 20375, USA

<sup>10</sup> Department of Physics and Astronomy, Amherst College, C025 New Science Center, 25 East Dr., Amherst, MA 01002-5000, USA

Received 20 September 2022 / Accepted 4 November 2022

## ABSTRACT

**Context.** During the third all-sky survey (eRASS3), eROSITA, the soft X-ray instrument aboard *Spectrum-Roentgen-Gamma*, detected a new hard X-ray transient, eRASSt J040515.6–745202, in the direction of the Magellanic Bridge.

**Aims.** We arranged follow-up observations and searched for archival data to reveal the nature of the transient.

**Methods.** Using X-ray observations with *XMM-Newton*, *NICER*, and *Swift*, we investigated the temporal and spectral behaviour of the source for over about 10 days.

**Results.** The X-ray light curve obtained from the *XMM-Newton* observation with an  $\sim 28$  ks exposure revealed a type-I X-ray burst with a peak bolometric luminosity of at least  $1.4 \times 10^{37}$  erg s<sup>-1</sup>. The burst energetics are consistent with a location of the burster at the distance of the Magellanic Bridge. The relatively long exponential decay time of the burst of  $\sim 70$  s indicates that it ignited in a H-rich environment. The non-detection of the source during the other eROSITA surveys, twelve and six months before and six months after eRASS3, suggests that the burst was discovered during a moderate outburst which reached  $2.6 \times 10^{36}$  erg s<sup>-1</sup> in persistent emission. During the *NICER* observations, the source showed alternating flux states with the high level at a similar brightness as during the *XMM-Newton* observation. This behaviour is likely caused by dips as also seen during the last hour of the *XMM-Newton* observation. Evidence for a recurrence of the dips with a period of  $\sim 21.8$  hr suggests eRASSt J040515.6–745202 is a low-mass X-ray binary (LMXB) system with an accretion disk seen nearly edge on. We identify a multi-wavelength counterpart to the X-ray source in UVW1 and g, r, i, and z images obtained by the optical/UV monitor on *XMM-Newton* and the Dark Energy Camera at the Cerro Tololo Inter-American Observatory. The spectral energy distribution is consistent with radiation from an accretion disk which dominates the UV and from a cool late-type star detected in the optical to infrared wavelengths.

**Conclusions.** After the discovery of X-ray bursts in M 31, the Magellanic Bridge is only the second location outside of the Milky Way where an X-ray burster was found. The burst uniquely identifies eRASSt J040515.6–745202 as an LMXB system with a neutron star. Its location in the Magellanic Bridge confirms the existence of an older stellar population which is expected if the bridge was formed by tidal interactions between the Magellanic Clouds, which stripped gas and stars from the clouds.

**Key words.** Galaxies: Magellanic Clouds – X-rays: binaries – X-rays: bursts – Stars: neutron – Stars: low-mass – X-rays: individual: eRASSt J040515.6–745202

## 1. Introduction

Type-I X-ray bursts are observed from low-mass X-ray binaries (LMXBs) and they uniquely identify the compact object in the system as a neutron star. The bursts occur when a sufficiently large amount of matter rich in H and He, which is accreted from the companion star, is gathered on the surface of the neutron star to ignite a thermonuclear runaway. Depending on the accretion rate, most bursts repeat on timescales of hours to days and typically last from  $\sim 10$  s to minutes. A few bursts were observed with much longer durations between several hours and a day. These very rare superbursts with a long recurrence time are thought to burn carbon, rather than the H-He fuel for short bursts (for reviews, see Galloway & Keek 2021; Parikh et al.

2013; Strohmayer & Bildsten 2006; Lewin et al. 1993). Temporal and spectral properties of a large sample of more than 7000 bursts from 85 bursting sources are described in Galloway et al. (2020).

The first type-I X-ray bursts outside of the Milky Way were detected in the Local Group galaxy M 31 using *XMM-Newton* data (Pietsch & Haberl 2005). The authors found two bursts, which were significantly detected in at least two of the EPIC instruments (Strüder et al. 2001; Turner et al. 2001). In a systematic search for fast transients in *XMM-Newton* EPIC-pn observations, Pastor-Marazuela et al. (2020) reported the identification of four bursts in the direction of M 31. The first burst in their Table 6 is identical to the second burst reported by Pietsch

& Haberl (2005)<sup>1</sup>. The other three bursts are new, thus increasing the number of X-ray bursters known in M 31 to five.

In the course of our X-ray source population studies of the Large and Small Magellanic Cloud (LMC and SMC) with eROSITA, we also monitored the Magellanic Bridge between the two satellite galaxies of the Milky Way. Together with the Magellanic Clouds, the Magellanic Bridge is part of a gaseous structure around the Magellanic Clouds spanning 200 degrees on the sky in total, also including a leading arm and a trailing stream (Nidever et al. 2010). The Magellanic Bridge consists of neutral gas and a young stellar component (Irwin et al. 1990). Moreover, Bagheri et al. (2013) found evidence for an older stellar population. Such a population is expected if the bridge was formed by tidal interactions between the LMC and SMC, which stripped gas and stars from the clouds (Mathewson 1985).

During the third 6 month long all-sky survey (eRASS3), the eROSITA instrument (Predehl et al. 2021) on board the Russian/German *Spektrum-Roentgen-Gamma* (SRG) mission (Sunyaev et al. 2021) discovered a new hard X-ray transient, designated eRASStJ040515.6–745202 (Rau et al. 2021). The source is located in the direction of the Magellanic Bridge, was not detected in eRASS1 nor eRASS2, and had faded again below the detection limit in eRASS4. Here, we report on X-ray and UV follow-up observations of eRASStJ040515.6–745202 with *XMM-Newton*, *Swift*, and *NICER*. An optical identification is provided from Dark Energy Camera (DECam) archival exposures.

## 2. X-ray observations

### 2.1. eROSITA

After its launch in July 2019, eROSITA started to scan the sky in December 2019 and completed four full sky surveys (eRASS1 to eRASS4) by December 2021. eROSITA consists of seven co-aligned Wolter type-I telescopes, each equipped with a camera based on a charge coupled device (CCD) of pn type with an integration time of 50 ms (Predehl et al. 2021).

eROSITA scanned eRASStJ040515.6–745202 eleven times during eRASS3 between 2021 May 1, 01:51 (MJD 59335.07738) and 2021 May 2, 17:52 (MJD 59336.74441; see Fig. 1). For the data analysis, we used the eROSITA Standard Analysis Software System (eSASS version eSASSUsers\_211214\_0\_3; Brunner et al. 2022). To extract source and background events for light curves and spectra, we used the eSASS task srctool (see e.g. Maitra et al. 2021; Haberl et al. 2022). We used circular regions with radii of 90'' and 120'' around the position of the source and a nearby source-free region, respectively, and selected all valid pixel patterns (PATTERN=15). For the light curves, we combined the data from all cameras (telescope modules TM 1–7) and applied a cut in the fractional exposure of 0.15 (FRACEXP>0.15) to exclude data from the edge of the detectors. We created a combined spectrum from the data of TMs 1–4 & 6, the five cameras with an on-chip optical blocking filter, with an average exposure time of 294 s. TM5 and TM7 suffer from a light leak (Predehl et al. 2021) and no reliable energy calibration is available yet.

### 2.2. Swift

Following the eROSITA discovery of eRASStJ040515.6–745202 (Rau et al. 2021), we initiated

<sup>1</sup> This was probably not recognised because a wrong observation ID was given by Pietsch & Haberl (2005) in the caption of their Fig. 4.

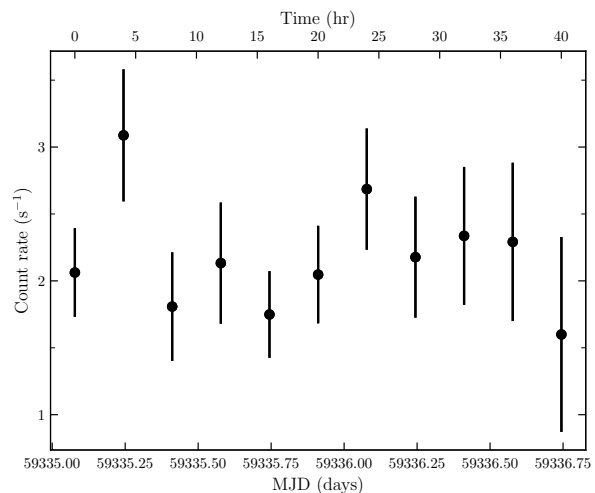


**Fig. 1.** Background-subtracted eROSITA light curve of eRASStJ040515.6–745202 during eRASS3 in the energy band 0.2–8.0 keV. Each data point represents one scan with a typical duration of 40 s and combines data from all seven cameras. The count rates were corrected for vignetting and point-spread function losses. The time in hours starts at the beginning of the first scan.

follow-up target of opportunity observations with the Neil Gehrels Swift Observatory (Gehrels et al. 2004). We used the data obtained from the X-ray telescope (XRT) in photon counting mode with a time resolution of 2.5 s. The observations were performed on 2021 May 12 and a total XRT exposure time of 1682 s was obtained. The XRT data were analysed using standard procedures (Evans et al. 2007, 2009).

### 2.3. XMM-Newton

To investigate the nature of eRASStJ040515.6–745202, we triggered one of our *XMM-Newton* anticipated target of opportunity observations (PI FH) to follow up on new hard transient sources in the Magellanic system. For this purpose, we utilised data from the European Photon Imaging Camera (EPIC), sensitive to the 0.15–12 keV band. Two of the three *XMM-Newton* telescopes are equipped with Metal Oxide Semi-conductor (MOS) CCD arrays (Turner et al. 2001) and the third with a pn-CCD (a predecessor of the eROSITA CCDs; Strüder et al. 2001). The observation was performed on 2021 May 14 (observation ID 0860800401, start MJD = 59348.0497). We used the cameras with medium optical blocking filters, EPIC-pn in large-window readout mode (48 ms time resolution), and EPIC-MOS in full-frame mode (2.6 s). We obtained net exposure times of 25.7 ks and 27.9 ks for EPIC-pn and EPIC-MOS, respectively, after we removed intervals of high background flaring activity, which occurred only at the end of the observation.

*XMM-Newton*/EPIC data were processed using the *XMM-Newton* data analysis software SAS, version 19.1.0<sup>2</sup>. We used the SAS task evselect for event extraction from circular regions around the source (45'' radius) and nearby background (60'' radius). Events with PATTERN 1–4 for EPIC-pn (Strüder et al. 2001) and PATTERN 1–12 for EPIC-MOS (Turner et al. 2001) were selected. We created light curves in the energy bands 0.2–2.2 keV, 2.2–8.0 keV, and 0.2–8.0 keV, applying the standard filtering with flags #XMMEA\_EP and #XMMEA\_EM for EPIC-pn and EPIC-MOS, respectively. For spectra we used the conser-

<sup>2</sup> Science Analysis Software (SAS): <http://xmm.esac.esa.int/sas/>

vative FLAG=0 filtering and created response files using the SAS tasks `arfgen` and `rmfgen`. As the best X-ray source position, we used the one derived by the *XMM-Newton* pipeline of  $\alpha_{J2000.0} = 04^{\text{h}} 05^{\text{m}} 14.^{\text{s}}96$  and  $\delta_{J2000.0} = -74^{\circ} 52' 01''.8$  with a  $1\sigma$  statistical uncertainty of  $0''.04$  and a remaining systematic error of  $0''.91$  after astrometric correction.

## 2.4. NICER

The *NICER* X-ray Timing Instrument (XTI, Gendreau et al. 2012, 2016) is a non-imaging, soft X-ray telescope on board the *International Space Station* (ISS). The XTI consists of an array of 56 co-aligned concentrator optics, each associated with a silicon drift detector (Prigozhin et al. 2012), operating in the 0.2–12 keV band. The XTI provides high time resolution ( $\sim 100$  ns) and spectral resolution of  $\sim 85$  eV at 1 keV. It has a field of view of  $\sim 30$  arcmin<sup>2</sup> in the sky and an effective area of  $\sim 1900$  cm<sup>2</sup> at 1.5 keV (with 52 active detectors).

For the current study, we used *NICER* data obtained between MJD 59339 and 59346 (i.e. before the *XMM-Newton* observation) which were grouped into six observation intervals (observation IDs 4570010101–6). Data were analysed with HEASOFT version 6.29c, *NICER* DAS version 2020-04-23\_V007a, and the calibration database (CALDB) version 20200722 (redistribution matrix and ancillary response files). For event selection and background filtering, we used standard screening criteria and intervals with magnetic cut-off rigidity between 1–15 GeV/c. Since *NICER* is not an imaging instrument, the X-ray background must be calculated from a database of data collected from empty background fields. The ‘space weather’ method (Gendreau et al., in prep.) contains functions which can be used to create the background spectrum based on estimates of the space weather environment. On the other hand, the 3C50 tool (Remillard et al. 2022) uses a number of background proxies from each *NICER* observation to define the basis states of the background database. We opted to use the latter since, for observations in the direction of the Magellanic Clouds, it has been shown to produce better estimates of the background (Treiber et al. 2021). After filtering the data, we were left with an exposure of  $\sim 12.8$  ks.

## 3. X-ray data analysis

### 3.1. Temporal analysis

The background-subtracted 0.2–8.0 keV light curves of eRASStJ040515.6–745202 obtained from the three EPIC instruments are shown in the upper part of Fig. 2. A short flare-like feature is consistently seen in all three light curves, with a fast rise and exponential decay as it is demonstrated in the zoom-in in the lower part of Fig. 2. A hardness ratio (HR) derived from the light curves in the soft (0.2–2.2 keV) and hard (2.2–8.0 keV) energy bands exhibits a similar rise and decay as the flux of the flare (Fig. 3). An investigation of the burst light curve (0.2–8 keV, total EPIC count rate) at higher time resolutions down to 1 s allowed us to estimate the rise time to  $\sim 7$ –10 s. The flux rise appears linear without significant dips, indicating the absence of photospheric radius expansion. Also, no significant HR variations are seen around the burst peak at 10 s time resolution and the statistics does not allow for this to be resolved better.

The temporal and spectral evolution (seen through the HR) of the flare is consistent with that of a type-I X-ray burst seen from LMXBs. These bursts are mainly detected from LMXBs in the Galaxy with various observatories, which allows for their

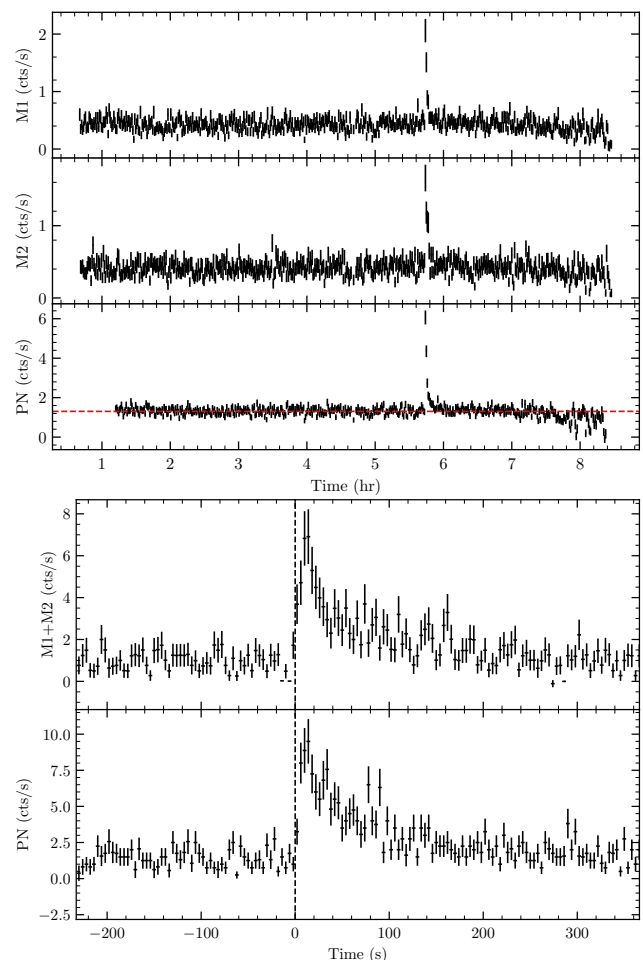


**Fig. 2.** Top: Background-subtracted EPIC-MOS1, MOS2, and pn light curves of eRASStJ040515.6–745202 in the energy band 0.2–8.0 keV with time bins of 50 s. Time zero corresponds to 2021 May 14 00:39:53 UT. The red dashed line marks the average count rate obtained from the full EPIC-pn light curve. Bottom: Zoom-in showing the X-ray burst with a time binning of 4 s. The light curves for MOS1 and MOS2 were summed up to gain statistics. Time zero corresponds to the burst onset (start of first bin with a significantly increased count rate).

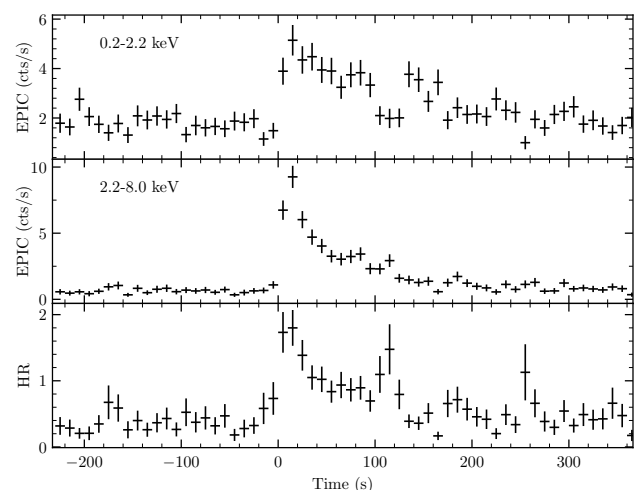


**Fig. 3.** Background-subtracted EPIC light curves (here MOS1, MOS2, and pn count rates are summed up) of eRASStJ040515.6–745202 in two energy bands with time bins of 10 s, together with the hardness ratio (count rate in the hard band divided by the count rate in the soft band) in the bottom panel. Time zero corresponds to the burst onset, as in Fig. 2

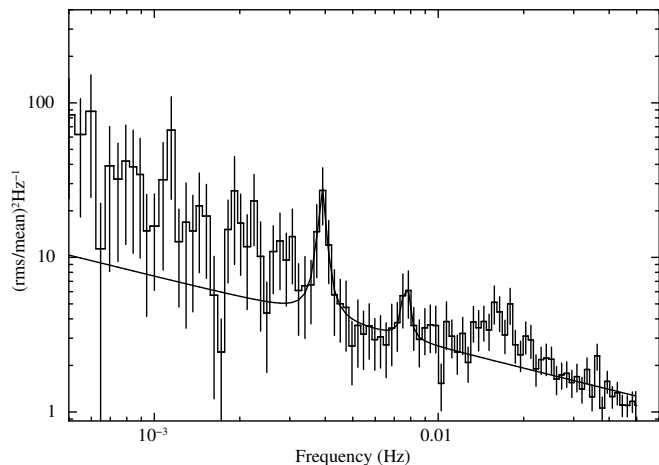


**Fig. 4.** PDS of eRASSt J040515.6–745202 produced from the EPIC-pn light curve in the energy range of 0.2–8 keV as a histogram with error bars. The solid line represents a model fit with a power law and two Lorentzian line profiles.

spectral evolution with high time resolution to be investigated (e.g. Keek et al. 2018; Degenaar et al. 2016; Chelovekov et al. 2005; Haberl et al. 1987; Swank et al. 1977).

Apart from the burst, the EPIC light curves show a dipping behaviour during the last  $\sim 1$  hr of the observation. The dips typically last 150–200 s and reach minima, which are consistent with zero flux. The dips are more pronounced in the 0.2–2.2 keV band, which results in increased HR. This is indicative of absorption as the origin for the dips.

We created power density spectra (PDS) for both the burst and quiescent intervals from the above light curves which were divided into segments of 4096 s with a time resolution of 10 s. The PDS obtained from all these segments were rebinned with a geometric rebinning factor and averaged to produce the final PDS. The average PDS was also normalised such that its integral gives the squared rms fractional variability and the expected white noise level was subtracted. The PDS from the quiescent interval shows two putative quasi-periodic oscillations (QPOs) at  $\sim 3.8$  mHz and its harmonic at  $\sim 7.6$  mHz as seen in Fig. 4. We fitted the PDS with a power-law component corresponding to the continuum and fitted the QPO features with two Lorentzian functions. The detection significance of the fundamental frequency is  $2.4\sigma$ , a quality factor ( $\nu/\text{FWHM}$ ) of  $\sim 14$ , and an rms fractional variability of  $\sim 3\%$  in the 0.2–8 keV range. The phenomenon of millihertz oscillations has been reported from a small subset of bursters at low frequencies ( $\approx 7$ –10 mHz) with an rms variability of  $\sim 2$ –3% and it can be associated with the transition from stable to unstable nuclear burning, or with the regime of marginally stable nuclear burning (see e.g. Revnivtsev et al. 2001; Heger et al. 2007). Millihertz QPOs are observed to be suppressed after an X-ray burst before they reappear later (Lyu et al. 2014). Hence, we created separate PDS from the persistent emission before and after the burst. Unfortunately, the statistics in the two parts is insufficient to detect the QPOs.

In Fig. 5 we show the *NICER* X-ray light curve that is used to further investigate the variability of the source. One can clearly recognise a few low-flux states that sporadically occur. The source seems to transition between a high and a low state as it can be seen by the histogram distribution of the count rate. The low state may be defined by the 0.5–1.2 cts  $\text{s}^{-1}$  intensity range.

We searched for a possible periodic nature of the dips on short ( $< 20$  ks) and longer (20–200 ks) timescales. For short timescales, we used the *NICER* light curve with photons grouped into 10 s bins, and we applied a method based on the phase dispersion minimisation test described by Stellingwerf (1978), which has been effectively applied to light curves of other sources (e.g. Vasilopoulos et al. 2021). We found hints of a periodic nature at a period of  $\sim 6$  ks and its harmonic. However, the low states could not be completely disentangled from the high (normal) state as seen in Fig. 6.

Power spectra of the EPIC light curves, which cover the full frequency range between  $\sim 4 \times 10^{-5}$  Hz (limited by the observation length) and  $\sim 10$  Hz (constrained by the EPIC-pn time resolution), do not show evidence for any significant signal near 6 ks ( $1.7 \times 10^{-4}$  Hz) nor at the highest frequencies. For longer timescales, we found that the Lomb-Scargle periodogram (Lomb 1976; Scargle 1982) was more effective. We applied the method following VanderPlas (2018) to the *NICER* light curve. We experimented with various bin sizes between 10 s and 300 s, which yielded consistent results. The periodogram revealed peaks at  $\sim 78.5$  ks and its harmonic (Fig. 7, top). We folded the *NICER* light curve for periods of 78 ks and 79 ks as shown in the bottom of Fig. 7. The phases covered by the *XMM-Newton* observation are indicated at the top of the plots. For the case of a period of 78 ks, dips are expected at the end of the *XMM-Newton* observation as they are observed (Fig. 2). In particular, from the EPIC light curves, it is evident that the associated decrease in flux does not follow the pattern expected from total or partial eclipses, but it more so resembles a dipping behaviour.

Finally, we investigated the *NICER* data for possible X-ray bursts using 5 s and 10 s time bins, but no bursts were identified. This is not unexpected since the combined duration of the *NICER* exposures is shorter than the *XMM-Newton* observation.

### 3.2. Spectral analysis

Analysis of the X-ray spectra was performed using XSPEC v12.10.1f (Arnaud 1996). For the spectral analysis of the burst, we extracted EPIC spectra from the quiescent emission of the full observation, excluding a  $\sim 3100$  s interval around the burst (source spectra binned to a minimum of 20 counts per bin to use Gaussian statistics), and spectra from the burst starting with burst rise and exposure times of 166 s (pn) and 174 s (MOS) (binned to a minimum of 1 count to use Cash statistics, Cash 1979). The number of extracted source counts during the burst is  $\sim 1200$  counts from all three instruments together, which did not allow us to monitor spectral evolution during the burst. To investigate the burst spectra, we first fitted the (background-subtracted) quiescent emission using a two-component model comprised of a power law and a disk blackbody, both attenuated by photo-electric absorption along the line of sight. The spectra with the best-fit model are presented in Fig. 8 with the corresponding model parameters listed in Table 1. For the fit to the burst spectra, the persistent emission components were included in the model with fixed parameters as derived above, that is to say we assume that the persistent emission did not change during the burst (however, see Worpel et al. 2013; Degenaar et al. 2016). For simplicity, we also adopted that the burst and persistent emission were attenuated by the same absorption. The derived  $N_{\text{H}}$  value of  $\sim 11.5 \times 10^{20} \text{ cm}^{-2}$  is somewhat larger than the Galactic foreground  $\text{H I}$  value of  $8.4 \times 10^{20} \text{ cm}^{-2}$  (Dickey & Lockman 1990) and consistent with  $10.5 \times 10^{20} \text{ cm}^{-2}$  as derived from the HI4PI map in this direction (HI4PI Collaboration et al. 2016) or  $13.9 \times 10^{20} \text{ cm}^{-2}$  when accounting for the contribution

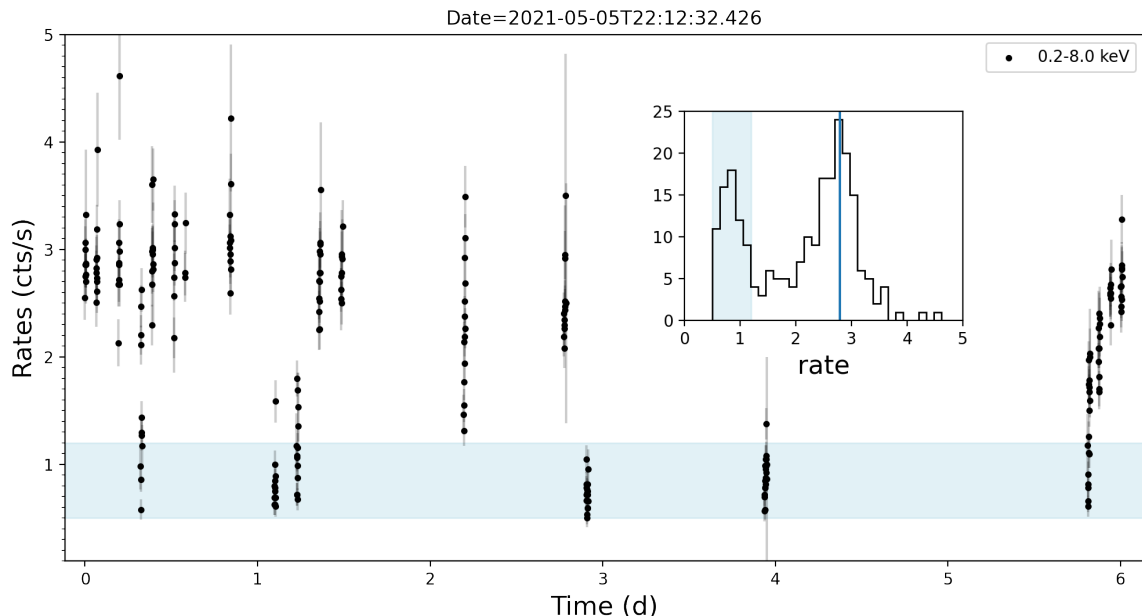


**Fig. 5.** *NICER* X-ray light curve in the 0.2–8.0 keV energy band using 64 s bins. The distribution of fluxes (shown in the inset) is clearly bimodal, with six low-flux states identified as shown in the shaded region (i.e. 0.5–1.2 cts s<sup>-1</sup>).

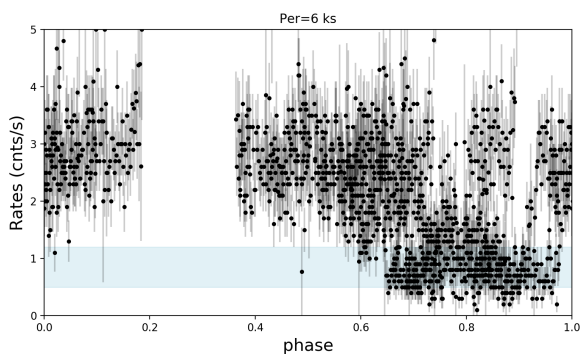


**Fig. 6.** *NICER* light curve (10 s bins) folded for a period of 6 ks. The shaded region marks the low-flux states as in Fig. 5.

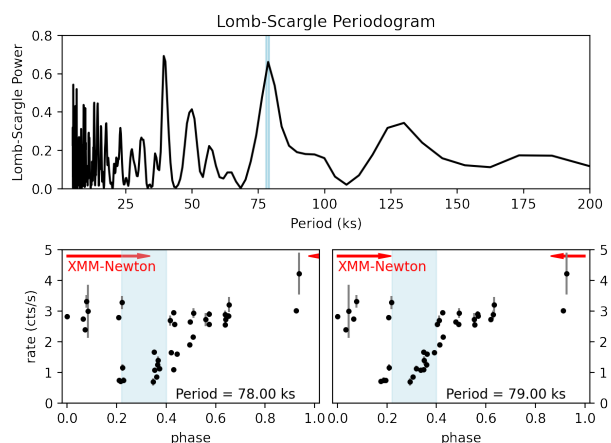


**Fig. 7.** Top: Lomb-Scargle periodogram of *NICER* data, a peak is visible at a period of 79 ks. Bottom: *NICER* light curve (300 s bin) folded for a period of 78 ks (left) and 79 ks (right). With red arrows, we mark the duration of the *XMM-Newton* observation. The shaded region in phase outlines the low-flux states as shown in Fig. 5.

of H<sub>2</sub> (Willingale et al. 2013). The latter values include the H I emission of the Galactic foreground and the Magellanic Bridge (see also Sasaki et al. 2022). If the absorption mainly originates in the interstellar medium, the column density determined from the X-ray spectra suggests a location of the source in the Magellanic Bridge.

For the burst emission, we started with a single blackbody component, which formally yielded an acceptable fit (C-statistic 758 for 951 dof), but it showed systematic residuals. Therefore, we added a second blackbody component to account for the cooling during the burst decay, as indicated by the hardness ratio (Fig. 3). The burst spectra with the best-fit model (C-statistic 741 for 949 dof) are presented in Fig. 9. For the temperatures, values of  $kT_1 = 1.55^{+0.20}_{-0.16}$  keV and  $kT_2 = 0.23^{+0.11}_{-0.07}$  keV were obtained. These two emission components dominate the spectrum at high and low energies, respectively (see Fig. 9). The observed average burst flux in the 0.2–10 keV band was  $1.65 \times 10^{-11}$  erg cm<sup>-2</sup> s<sup>-1</sup>, which corresponds to an absorption-corrected X-ray luminosity of  $6.2 \times 10^{36}$  erg s<sup>-1</sup>, assuming a distance of 55 kpc (be-

tween that of the SMC and LMC). The bolometric luminosities inferred from the two blackbody normalisations are  $6.54 \times 10^{36}$  erg s<sup>-1</sup> and  $0.33 \times 10^{36}$  erg s<sup>-1</sup> for the high- and low-temperature component, respectively, which yield a total average bolometric burst luminosity of  $6.87 \times 10^{36}$  erg s<sup>-1</sup>. The average EPIC count rate over the 170 s burst interval inferred from the light curve with a 4 s binning (Fig. 2) was 6.86 cts s<sup>-1</sup>, while the maximum reached  $16.1 \pm 1.9$  cts s<sup>-1</sup>. This implies a bolometric luminosity at a burst peak of at least  $1.4 \times 10^{37}$  erg s<sup>-1</sup>, but probably higher because the burst peak is not resolved with 4 s bins. The apparent emission radii for the two blackbody components, assuming spherical emission, are  $R_1 = 3.0 \pm 0.5$  km and  $R_2 = 31^{+30}_{-16}$  km.

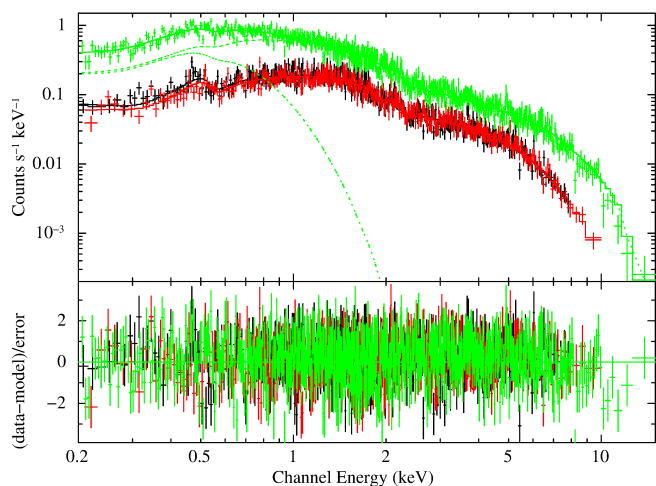


**Fig. 8.** EPIC spectra of the persistent emission from eRASSJ040515.6–745202 (MOS1, black; MOS2, red; and pn, green) extracted from the full observation, excluding the burst interval. The best-fit model consisting of a disk-blackbody and a power-law component is plotted as histogram. The two emission components are indicated as dotted lines (for better visibility for the pn spectrum only). The bottom panel shows the residuals.

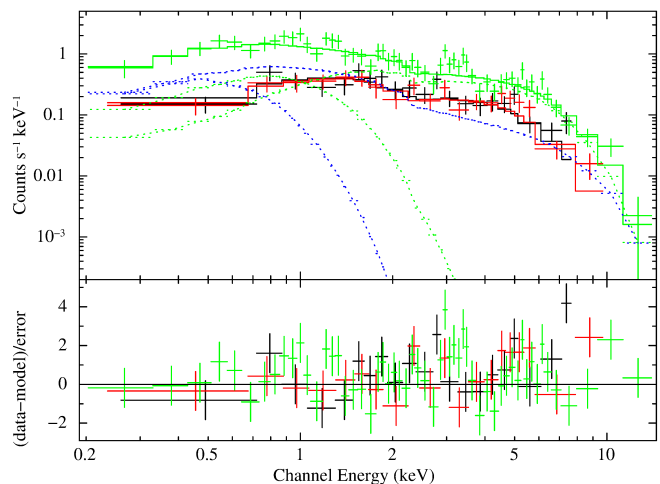


**Fig. 9.** EPIC spectra of the X-ray burst seen from eRASSJ040515.6–745202 (MOS1, black; MOS2, red; and pn, green). The best-fit model consists of two blackbody emission components in addition to the persistent emission. The best-fit model is plotted as a histogram. The two blackbody burst emission components are indicated as green dotted lines and the two components of the persistent emission as blue dotted lines (for better visibility for the pn spectrum only). The bottom panel shows the residuals.

However, it should be noted that these can only be treated as a rough estimate because they were derived from a spectrum averaged over the burst which is expected to show large temperature variations during its time evolution.

To approximate a multi-temperature spectrum, we used a disk-blackbody model with a power-law distribution of the temperature (diskpbb in XSPEC). Although this model is not physical for an application to a temperature decrease with time (which is likely more exponential), it probably allows us to better estimate the maximum temperature. In the two-blackbody model, the temperatures only provide averages over a certain time interval during the burst decay. The diskpbb model yields a similar fit quality (C-statistic of 747 for 950 dof, with one free parameter less than for the two-blackbody model) with a maximum  $kT = 2.9_{-0.8}^{+1.4}$  keV. Peak temperatures above 2 keV are typically observed from known bursters (70% of the bursts have a peak  $kT > 2$  keV, Galloway et al. 2020).

We fitted the *NICER* spectra with a similar persistent-emission model to look for possible spectral evolution. Given the nature of the *NICER* background, we performed the fitting using PG statistics within XSPEC, which implements Cash statistics (Cash 1979), with a non-Poisson background model<sup>3</sup>. To maximise signal-to-noise, we only fitted *NICER* data of the high (normal) state (i.e. exposure of 8 ks). Data were initially fitted by an absorbed power law while a soft disk blackbody was added to account for residuals at low energies. Best-fit (PG statistics of 880 for 764 dof) parameter values are given in Table 1, while the best-fit model is plotted in Fig. 10.

We then compared the intensity of the low states seen in the *NICER* light curve with the *NICER* background level. For that, we extracted source and background spectra using the respective time intervals. This resulted in a net count rate of 0.66 cts s<sup>-1</sup> and a background of 0.57 cts s<sup>-1</sup>, using the 3C50 model. Consequently, the low states are marginally brighter than the background level, and the source almost fades away during these intervals.

<sup>3</sup> <https://heasarc.gsfc.nasa.gov/xanadu/xspec/manual/XSappendixStatistics.html>

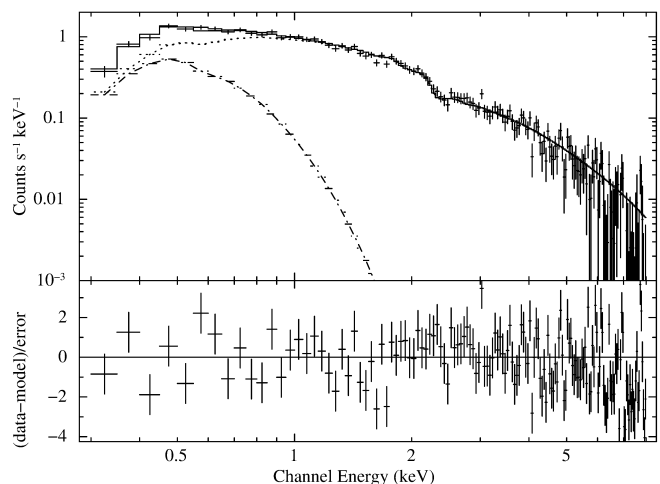


**Fig. 10.** *NICER* spectrum of the high (normal) state (i.e. count rate  $> 1.5$  cts s<sup>-1</sup>). As for Fig. 8, the contributions of disk blackbody (dash-dotted) and power law (dotted) are shown separately.

We also fitted the eROSITA spectrum with the two-component model of a power law and disk blackbody. Because the statistical quality of the spectrum is too low to justify a fit with so many degrees of freedom, we fixed the  $N_H$  at the average value obtained from the EPIC and *NICER* spectra. The spectrum with the best-fit model is presented in Fig. 11. For the model parameters, readers can refer to Table 1. The disk-blackbody temperature derived from the eROSITA spectrum is lower than that found from the EPIC and *NICER* spectra, which may be caused by the higher low-energy contribution of the steeper power law. Fixing either the power-law index or the temperature at the EPIC/*NICER* average values, however, does not bring the corresponding parameter in agreement, indicating a somewhat lower contribution of the disk component during the eROSITA observations. We note that the spectral model used by Rau et al. (2021) includes a blackbody component instead of a disk blackbody. This has the effect that in their spectral fit, the steeper power law

**Table 1.** Results of spectral fits to the X-ray spectra of the persistent emission.

Instrument	$N_{\text{H}}/10^{20}$ <sup>(a)</sup> ( $\text{cm}^{-2}$ )	kT (eV)	$\Gamma$	C/PG-stat	$\chi^2$	dof	$F_{\text{obs}}/10^{-12}$ <sup>(b)</sup> ( $\text{erg cm}^{-2} \text{s}^{-1}$ )	$L/10^{36}$ <sup>(c)</sup> ( $\text{erg s}^{-1}$ )	$R_{\text{in}} \times \sqrt{\cos \theta}$ <sup>(d)</sup> (km)
EPIC	$11.3 \pm 1.9$	$142^{+15}_{-12}$	$1.42 \pm 0.03$	–	1404	1405	$5.83 \pm 0.12$	$2.63 \pm 0.07$	$74^{+29}_{-22}$
NICER	$11.7^{+2.4}_{-2.1}$	$129^{+17}_{-18}$	$1.41^{+0.05}_{-0.05}$	880	1416	764	$5.93^{+0.2}_{-0.22}$	$2.61^{+0.15}_{-0.13}$	$80^{+50}_{-40}$
eROSITA	11.5 fix	$44^{+67}_{-25}$	$1.81^{+0.44}_{-0.42}$	89.3	94.5	132	$4.06^{+2.04}_{-1.30}$	$1.75^{+5.97}_{-1.56}$	$4260^{+11600}_{-4130}$
Swift/XRT	11.5 fix	–	$1.64^{+0.21}_{-0.21}$	86.8	106.6	120	$5.2^{+0.6}_{-0.7}$	$2.3^{+0.4}_{-0.3}$	–

**Notes.** Best-fit parameters for an absorbed two-component model consisting of disk-blackbody and power-law emission. Errors indicate 90% confidence ranges. <sup>(a)</sup> For the photo-electric absorption by gas along the line of sight, we used `tbabs` in XSPEC with interstellar abundances following Wilms et al. (2000) and atomic cross sections from Verner et al. (1996). <sup>(b)</sup> Observed flux in the 0.2–10.0 keV energy band. <sup>(c)</sup> Source-intrinsic luminosity corrected for absorption and assuming a distance of 55 kpc (0.2–10.0 keV). <sup>(d)</sup> Inner radius of the accretion disk with inclination angle  $\theta$ .

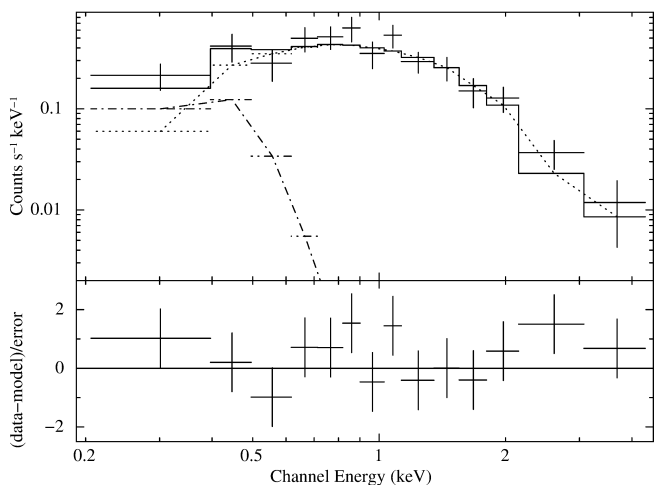


**Fig. 11.** eROSITA spectrum obtained from eRASS3. The best-fit model consists of a disk-blackbody (dash-dotted) and a power-law (dotted) component as used for the persistent emission seen during the *XMM-Newton* observation.

accounts for the soft part of the spectrum, while the hot blackbody represents the harder emission. In the model of this work, the role of the two emission components is reversed, which leads to the different best-fit parameters.

The source was detected with *Swift*/XRT with a net count rate of  $(0.094 \pm 0.008)$  cts  $\text{s}^{-1}$ . Given the small number of source counts ( $\sim 150$ ), spectra were binned to a minimum of 1 count per bin, while spectral fitting was performed based on Cash statistics. As for the fit to the eROSITA spectrum, the  $N_{\text{H}}$  was fixed to  $11.5 \times 10^{20} \text{ cm}^{-2}$ . A simple absorbed power-law model was adequate to explain the data (C-Statistics of 86.8 for 120 degrees of freedom, with a corresponding  $\chi^2$  of 106.6, Table 1). The power-law photon index had a value of  $\sim 1.6$ , consistent with what was derived from the other X-ray spectra, while the absorption-corrected X-ray luminosity was found to be  $\sim 2.3 \times 10^{36} \text{ erg s}^{-1}$  (0.2–10.0 keV), which is also in the range seen during the other observations.

#### 4. UV, optical, and near-infrared data

As described by Rau et al. (2021), *Swift* observed the region around eRASS J040515.6–745202 with the Ultra-Violet/Optical telescope (UVOT, Roming et al. 2005) and the

UVW1 filter<sup>4</sup> with an exposure time of 1754 s. We downloaded the *Swift*/UVOT data from the UK Swift Science Data Centre<sup>5</sup>, which includes the UVW1 image (shown in Fig. 12, left) and a source detection list produced by the data centre pipeline. Source magnitudes are given in the Vega system. The two UVOT sources listed in Rau et al. (2021) are not contained in this source list and are fainter than the faintest source (21.48 mag) in the list, indicating their lower significance.

The source region was also observed with the *XMM-Newton* optical/UV monitor telescope (OM; Mason et al. 2001), using the UVW1 filter<sup>6</sup> and the detector in fast imaging mode. The total exposure time was 20.98 ks, which is significantly higher than the UVOT exposure. We downloaded the pipeline products generated from the OM data from the *XMM-Newton* science archive<sup>7</sup>. The OM/UVW1 image is shown in Fig. 12 (right). UVOT source 1 is also detected in the OM image (source ID 44 in the OM detection list). Source 1 is ruled out in any case as the UV counterpart of eRASS J040515.6–745202 by the improved *XMM-Newton* position. A clear source (OM 42) is detected inside the  $2\sigma$  *XMM-Newton*/EPIC error radius with a UVW1 magnitude of  $21.68 \pm 0.08$ . It is located at R.A. =  $04^{\text{h}} 05^{\text{m}} 14^{\text{s}}.928$  and Dec. =  $-74^{\circ} 52' 00''.46$  (J2000) with a  $1\sigma$  error of  $0.19''$ .

Comparing OM and UVOT images (Fig. 12), UVOT source 2 might suffer from a cross-like feature, which is visible in the UVOT image. This could be caused by statistical background fluctuations due to the short exposure time or an independent transient source (at the position of UVOT 2) blended with OM 42. We regard OM source 42 as more reliable as its shape is mostly circular, which is consistent with the point spread function of the instrument. We found no counterpart at any wavelength within  $5''$  to OM source 42 using the VizieR catalogue access tool<sup>8</sup>.

An optical counterpart was identified in archival data from DECam (Flaugher et al. 2015), a wide-field CCD camera on the Blanco 4-m telescope at the Cerro Tololo Inter-American Observatory. Twenty-four exposures in g, r, i, and z filters from three programmes were used (including the DECam eROSITA Survey, DeROSITAS, an optical companion survey to the eROSITA survey). The exposures were instrumentally calibrated by the DECam Community Pipeline (Valdes 2021) and catalogued for the

<sup>4</sup> Bandwidth (full width at half maximum) of 69.3 nm with a central wavelength of 260 nm

<sup>5</sup> [https://www.swift.ac.uk/swift\\_portal/](https://www.swift.ac.uk/swift_portal/)

<sup>6</sup> Band width of 83 nm at an effective wavelength of 291 nm

<sup>7</sup> <https://www.cosmos.esa.int/web/xmm-newton/xsa>

<sup>8</sup> <http://cdsarc.u-strasbg.fr/viz-bin/VizieR>

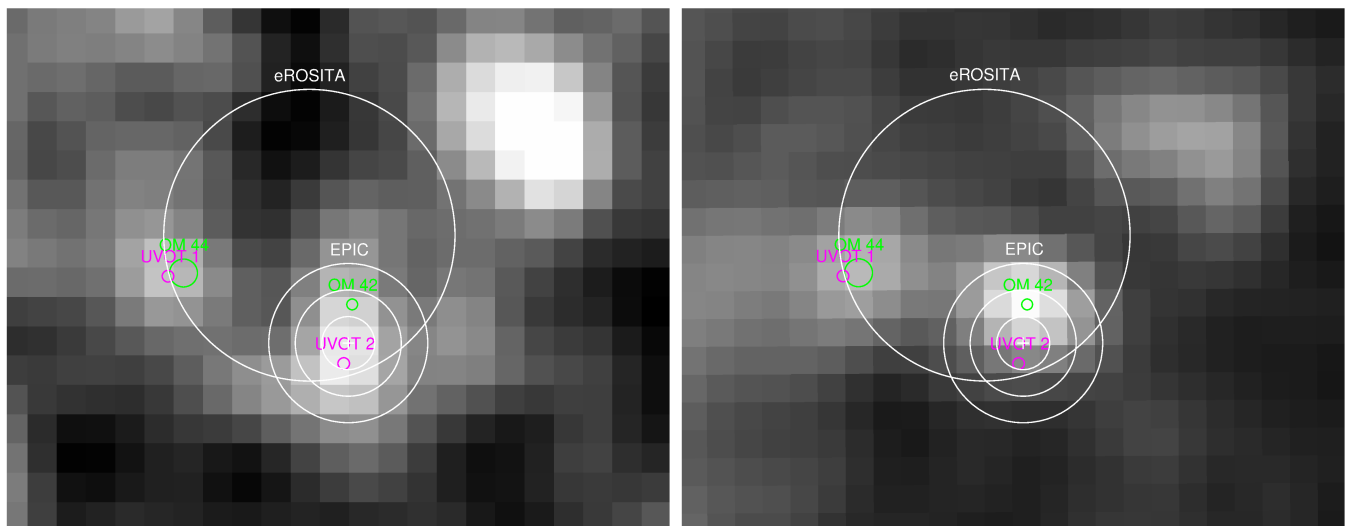


**Fig. 12.** UVW1-band images from *Swift*/UVOT (left) and *XMM-Newton*/OM. The large white circle (radius  $5''$ ) marks the eROSITA error circle from [Rau et al. \(2021\)](#), and the three concentric white circles indicate the 1, 2, and  $3\sigma$  position uncertainties obtained from the *XMM-Newton*/EPIC X-ray images. The magenta circles mark the positions of the UVOT sources given by [Rau et al. \(2021\)](#), and the green circles ( $1\sigma$  errors) indicate the sources detected in the *XMM-Newton*/OM UVW1 image.

Legacy Surveys’ ([Dey et al. 2019](#)) data release (DR10 in preparation). The analysis uses the Tractor ([Lang et al. 2016](#)) forward modelling method. The method fits models to the observations, taking the point spread functions from the exposures into account. The Tractor fitting agrees with both a very compact galaxy or a point source; that is to say, the data are consistent with either a slightly extended source or a star. The measured AB magnitudes, an absolute spectral flux density photometric system, are  $[24.08 \pm 0.11, 23.21 \pm 0.07, 23.05 \pm 0.05, 22.27 \pm 0.09]$  in  $[g, r, i, z]$ , respectively. The photometric calibration is tied to Pan-STARRS DR1 ([Chambers et al. 2016](#)) through an uber-cal self-calibration method ([Schlafly et al. 2012](#)). The images centred on the position obtained for the UV counterpart of eRASSt J040515.6–745202 are shown in Fig. 13.

## 5. Discussion

During our eROSITA project to identify hard X-ray transients in the Magellanic system, an alert was generated by the eROSITA Near-Real Time Analysis system ([Predehl et al. 2021](#)). The transient, eRASSt J040515.6–745202, was only detected during eRASS3 and is located in the direction of the Magellanic Bridge ([Rau et al. 2021](#)).

A follow-up observation with *XMM-Newton* revealed an X-ray burst with energetics that suggest the source is located at the distance of the Magellanic Bridge. Assuming a distance of 55 kpc (between that of the SMC and LMC), a burst peak bolometric luminosity of more than  $1.4 \times 10^{37}$  erg  $s^{-1}$  is derived, which is typical of most X-ray bursts. Given the large distance, the statistics is low; however, we can infer certain characteristics of the burst.

According to theory, type-I X-ray bursts, which are caused by unstable burning of the accreted matter, occur at certain mass accretion rates. Three different regimes are predicted which produce different types of X-ray bursts ([Bildsten 2000](#); [Fujimoto et al. 1981](#)).

1. mixed H/He burning triggered by thermally unstable H ignition at low accretion rates of  $10^{-14} M_{\odot} \text{ yr}^{-1} \lesssim \dot{M} \lesssim 2 \times 10^{-10} M_{\odot} \text{ yr}^{-1}$

$M_{\odot} \text{ yr}^{-1}$  resulting in a type I X-ray burst in a H-rich environment

2. pure He shell ignition after steady H burning at intermediate accretion rates of  $2 \times 10^{-10} M_{\odot} \text{ yr}^{-1} \lesssim \dot{M} \lesssim 4-11 \times 10^{-10} M_{\odot} \text{ yr}^{-1}$
3. mixed H/He burning triggered by thermally unstable He ignition at high accretion rates of  $4-11 \times 10^{-10} M_{\odot} \text{ yr}^{-1} \lesssim \dot{M} \lesssim 2 \times 10^{-8} M_{\odot} \text{ yr}^{-1}$

Moreover, sedimentation of heavy elements was suggested to play an important role for the burst environment. This can lead to additional burst regimes ([Peng et al. 2007](#)).

The critical accretion rates depend on metallicity, and in particular on the mass fraction of CNO ( $Z_{\text{CNO}} \sim 0.01$  for solar abundances). Between regime 1 and 2 the transition  $\dot{M}$  is modified by a factor of  $(Z_{\text{CNO}}/0.01)^{1/2}$ . For Magellanic Cloud metallicities between 0.2 (SMC) and 0.5 solar (LMC), the critical accretion rates are, therefore, lowered by about a factor of 0.45–0.71.

To convert the persistent luminosity of eRASSt J040515.6–745202 ( $2.6 \times 10^{36}$  erg  $s^{-1}$ ) to a mass accretion rate, we assumed standard neutron star parameters ( $1.4 M_{\odot}$ , a radius of 12 km, and a 100% efficiency for the conversion of potential energy into X-rays). This results in  $2.6 \times 10^{-10} M_{\odot} \text{ yr}^{-1}$ , which is somewhat above the critical rate between regime 1 and 2 where a He burst is expected for sub-solar metallicity.

Following [in’t Zand et al. \(2017\)](#), we fitted an exponential decay to the burst light curve (total EPIC count rate in the 0.2–8.0 keV band, Fig. 2). We find an exponential decay time of  $70.6^{+8.9}_{-7.6}$  s ( $1\sigma$  uncertainties). From the analysis of more than 1200 X-ray bursts, [in’t Zand et al. \(2017\)](#) find that the most common decay time is 5 s and only 1% have decay times longer than 70 s. For bursts driven by He burning, short ( $\sim 10$  s) decay times are expected ([Parikh et al. 2013](#)), suggesting that the observed burst from eRASSt J040515.6–745202 ignited in a H-rich environment. This is consistent with the recurrence time, which must be longer than 5.06 hr given by the constraint of the observation start. For He bursts, shorter recurrence times may be expected. For the  $\alpha$  value, the ratio between integrated fluxes of persistent emission between the burst and the previous one, and the



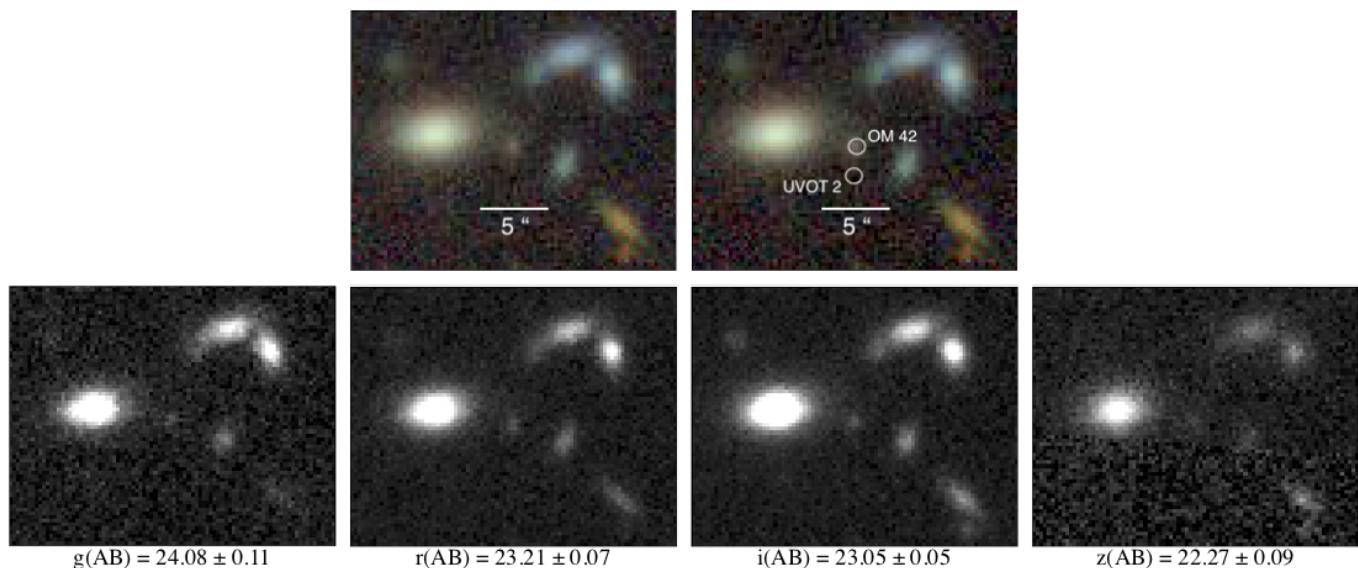


**Fig. 13.** Cutouts of the DECam imaging at the same size and position as Fig. 12. Each image is a coadd of many exposures in each filter and also rendered as a colour composite. The positions of OM source 42 and UVOT source 2 are overlaid in a copy of the composite for reference. The exposures used are public archival data included in the Legacy Surveys data release 10 (DR10).

burst emission, we can infer a lower limit of 38. In the simplest model, assuming isotropic emission and all accreted matter is processed during the bursts;  $\alpha$  values of  $\sim 30$  and  $\sim 120$  are expected for pure H and He burning, respectively. However, the picture is more complicated and  $\alpha$  values between 10 and 1000 were observed (Sect. 3.7 of Lewin et al. 1993).

eRASStJ040515.6–745202 was scanned by eROSITA for about two days each during four epochs separated by 0.5 year intervals. The only eROSITA detection on May 1–2, 2021 and during follow-up observations with *NICER* (May 5–12), *Swift* (May 12), and *XMM-Newton* (May 14) suggest that the source was in a moderate outburst, lasting at least two weeks. During this outburst, the accretion rate was sufficiently high to gather enough hydrogen for the ignition of an X-ray burst. On longer timescales, the source accretes at a much lower rate, which makes the detection of bursts in a typical X-ray follow-up observation very unlikely.

During the *NICER* observations, eRASStJ040515.6–745202 alternated between two flux states. The high-flux level was similar to the persistent emission seen during the *XMM-Newton* observation, while during low states the flux was typically a factor of 4–5 lower. These dips in the *NICER* light curve could be due to absorption or even eclipses similar to those found in other LMXBs observed with *NICER* (e.g. Homan et al. 2021; Buisson et al. 2021). The source also exhibited dipping behaviour for the last  $\sim 1$  hr of the *XMM-Newton* observation. The dips are resolved in the EPIC light curves, and they typically lasted for 150–200 s and reached minimum count rates consistent with zero. During the dips, the hardness ratio increased, which suggests they are the result of absorption and obscuration by optically thick material. As was proposed for other dipping LMXBs, this material is likely located in a thickened region of the accretion disk where the accretion flow from the secondary star impacts on the disk (Díaz Trigo et al. 2006). In systems with sufficiently high inclination, the neutron star then gets partially occulted by this region. From the *NICER* data, we find some evidence for a periodic nature of the dips with a period of around 78.5 ks (21.8 hr). Since the dips are not resolved in the *NICER* light

curves, the period remains uncertain, but the dip phases derived from the *XMM-Newton* observation are consistent with the *NICER*-derived period of 78–79 ks. With an orbital period of  $\sim 21.8$  hr, eRASStJ040515.6–745202 would be very similar to SwiftJ1858.6–0814 (orbital period 21.34 hr), which also exhibits X-ray bursts and dips and, in addition, eclipses with a 1.14 hr duration (Buisson et al. 2021; Knight et al. 2022). Eclipses could also be present in the *NICER* light curves of eRASStJ040515.6–745202, but the low count rate and the duration of *NICER* snapshots combined with the low number of visits makes it difficult to detect the ingress and egress of eclipses and differentiate them from dips. Considering the similarities with SwiftJ1858.6–0814, the dipping behaviour could also be due to disk outflows (Castro Segura et al. 2022).

The detection of a type-I X-ray burst uniquely characterises eRASStJ040515.6–745202 as an LMXB with the compact object identified as a neutron star. From UV, optical, and IR images, we identified the counterpart to the X-ray source with a spectral energy distribution suggesting two emission components. The flux measurements in the g, r, i, and z bands increase with wavelength, consistent with radiation from a late-type M star (effective temperature of around 3000 K). The contribution of such a star in the UV is negligible and the bright UV emission detected by the *XMM-Newton*/OM most likely originates from the accretion disk around the neutron star. An early-type OB star to account for the UV emission can definitely be ruled out as it would be expected to be brighter than  $\sim 16$ th magnitude in the optical B and V bands. This picture is fully consistent with the LMXB nature of the system and confirms the identification of the multi-wavelength counterpart to the X-ray source.

The only other LMXB known in the Magellanic System is LMC X-2, a persistently bright system in the southern part of the LMC (e.g. Agrawal & Nandi 2020; Smale & Kuulkers 2000; Bonnet-Bidaud et al. 1989). The location of LMC X-2 is outside the area where younger stellar populations are found, which are traced in X-rays by high-mass X-ray binaries (Haberl & Sturm 2016) and core-collapse supernova remnants (Maggi et al. 2016). eRASStJ040515.6–745202 is located even further out in the Magellanic Bridge, about one-third of the angular distance to

the SMC. The discovery of an LMXB in the Magellanic Bridge adds support to the existence of an old population (Bagheri et al. 2013) and hence the theory of tidal interaction.

*Acknowledgements.* This work is based on data from eROSITA, the soft X-ray instrument aboard *SRG*, a joint Russian-German science mission supported by the Russian Space Agency (Roskosmos), in the interests of the Russian Academy of Sciences represented by its Space Research Institute (IKI), and the Deutsches Zentrum für Luft- und Raumfahrt (DLR). The *SRG* spacecraft was built by Lavochkin Association (NPOL) and its subcontractors, and is operated by NPOL with support from the Max Planck Institute for Extraterrestrial Physics (MPE). The development and construction of the eROSITA X-ray instrument was led by MPE, with contributions from the Dr. Karl Remeis Observatory Bamberg & ECAP (FAU Erlangen-Nürnberg), the University of Hamburg Observatory, the Leibniz Institute for Astrophysics Potsdam (AIP), and the Institute for Astronomy and Astrophysics of the University of Tübingen, with the support of DLR and the Max Planck Society. The Argelander Institute for Astronomy of the University of Bonn and the Ludwig Maximilians Universität Munich also participated in the science preparation for eROSITA. The eROSITA data shown here were processed using the eSASS software system developed by the German eROSITA consortium. This work used observations obtained with *XMM-Newton*, an ESA science mission with instruments and contributions directly funded by ESA Member States and NASA. The *XMM-Newton* project is supported by the DLR and the Max Planck Society. Work on *NICER* science at NRL is funded by NASA and the Office of Naval Research. This research has made use of the VizieR catalogue access tool, CDS, Strasbourg, France (DOI: 10.26903/cds/vizie). The original description of the VizieR service was published in (Ochsenbein et al. 2000). We thank the anonymous referee for the very useful suggestions, which helped to improve the paper.

## References

- Agrawal, V. K. & Nandi, A. 2020, *MNRAS*, 497, 3726
- Arnaud, K. A. 1996, in *ASP Conf. Ser. 101: Astronomical Data Analysis Software and Systems V*, 17
- Bagheri, G., Cioni, M. R. L., & Napiwotzki, R. 2013, *A&A*, 551, A78
- Bildsten, L. 2000, in *American Institute of Physics Conference Series*, Vol. 522, *Cosmic Explosions: Tenth AstroPhysics Conference*, ed. S. S. Holt & W. W. Zhang, 359–369
- Bonnet-Bidaud, J. M., Motch, C., Beuermann, K., et al. 1989, *A&A*, 213, 97
- Brunner, H., Liu, T., Lamer, G., et al. 2022, *A&A*, 661, A1
- Buisson, D. J. K., Altamirano, D., Armas Padilla, M., et al. 2021, *MNRAS*, 503, 5600
- Cash, W. 1979, *ApJ*, 228, 939
- Castro Segura, N., Knigge, C., Long, K. S., et al. 2022, *Nature*, 603, 52
- Chambers, K. C., Magnier, E. A., Metcalfe, N., et al. 2016, *arXiv e-prints*, arXiv:1612.05560
- Chelovekov, I. V., Lutovinov, A. A., Grebenev, S. A., & Sunyaev, R. A. 2005, *Astronomy Letters*, 31, 681
- Degenaar, N., Koljonen, K. I. I., Chakrabarty, D., et al. 2016, *MNRAS*, 456, 4256
- Dey, A., Schlegel, D. J., Lang, D., et al. 2019, *AJ*, 157, 168
- Díaz Trigo, M., Parmar, A. N., Boirin, L., Méndez, M., & Kaastra, J. S. 2006, *A&A*, 445, 179
- Dickey, J. M. & Lockman, F. J. 1990, *ARA&A*, 28, 215
- Evans, P. A., Beardmore, A. P., Page, K. L., et al. 2009, *MNRAS*, 397, 1177
- Evans, P. A., Beardmore, A. P., Page, K. L., et al. 2007, *A&A*, 469, 379
- Flaugher, B., Diehl, H. T., Honscheid, K., et al. 2015, *AJ*, 150, 150
- Fujimoto, M. Y., Hanawa, T., & Miyaji, S. 1981, *ApJ*, 247, 267
- Galloway, D. K., in't Zand, J., Chenevez, J., et al. 2020, *ApJS*, 249, 32
- Galloway, D. K. & Keek, L. 2021, *Astrophysics and Space Science Library*, 461, 209
- Gehrels, N., Chincarini, G., Giommi, P., et al. 2004, *ApJ*, 611, 1005
- Gendreau, K. C., Arzoumanian, Z., Adkins, P. W., et al. 2016, *Society of Photo-Optical Instrumentation Engineers (SPIE) Conference Series*, Vol. 9905, *The Neutron star Interior Composition Explorer (NICER): design and development*, 99051H
- Gendreau, K. C., Arzoumanian, Z., & Okajima, T. 2012, *Society of Photo-Optical Instrumentation Engineers (SPIE) Conference Series*, Vol. 8443, *The Neutron star Interior Composition Explorer (NICER): an Explorer mission of opportunity for soft x-ray timing spectroscopy*, 844313
- Haberl, F., Maitra, C., Carpano, S., et al. 2022, *A&A*, 661, A25
- Haberl, F., Stella, L., White, N. E., Priedhorsky, W. C., & Gottwald, M. 1987, *ApJ*, 314, 266
- Haberl, F. & Sturm, R. 2016, *A&A*, 586, A81
- Heger, A., Cumming, A., & Woosley, S. E. 2007, *ApJ*, 665, 1311
- HI4PI Collaboration, Ben Bekhti, N., Flöer, L., et al. 2016, *A&A*, 594, A116
- Homan, J., Gendreau, K. C., Sanna, A., et al. 2021, *The Astronomer's Telegram*, 14606, 1
- in't Zand, J. J. M., Visser, M. E. B., Galloway, D. K., et al. 2017, *A&A*, 606, A130
- Irwin, M. J., Demers, S., & Kunkel, W. E. 1990, *AJ*, 99, 191
- Keek, L., Arzoumanian, Z., Chakrabarty, D., et al. 2018, *ApJ*, 856, L37
- Knight, A. H., Ingram, A., & Middleton, M. 2022, *MNRAS*, 514, 1908
- Lang, D., Hogg, D. W., & Mykytyn, D. 2016, *The Tractor: Probabilistic astronomical source detection and measurement*, *Astrophysics Source Code Library*, record ascl:1604.008
- Lewin, W. H. G., van Paradijs, J., & Taam, R. E. 1993, *Space Sci. Rev.*, 62, 223
- Lomb, N. R. 1976, *Ap&SS*, 39, 447
- Lyu, M., Méndez, M., & Altamirano, D. 2014, *MNRAS*, 445, 3659
- Maggi, P., Haberl, F., Kavanagh, P. J., et al. 2016, *A&A*, 585, A162
- Maitra, C., Haberl, F., Vasilopoulos, G., et al. 2021, *A&A*, 647, A8
- Mason, K. O., Breeveld, A., Much, R., et al. 2001, *A&A*, 365, L36
- Mathewson, D. S. 1985, *PASA*, 6, 104
- Nidever, D. L., Majewski, S. R., Butler Burton, W., & Nigra, L. 2010, *ApJ*, 723, 1618
- Ochsenbein, F., Bauer, P., & Marcout, J. 2000, *A&AS*, 143, 23
- Parikh, A., José, J., Sala, G., & Iliadis, C. 2013, *Progress in Particle and Nuclear Physics*, 69, 225
- Pastor-Marazuela, I., Webb, N. A., Wojtowicz, D. T., & van Leeuwen, J. 2020, *A&A*, 640, A124
- Peng, F., Brown, E. F., & Truran, J. W. 2007, *ApJ*, 654, 1022
- Pietsch, W. & Haberl, F. 2005, *A&A*, 430, L45
- Predehl, P., Andritschke, R., Arefiev, V., et al. 2021, *A&A*, 647, A1
- Prigozhin, G., Gendreau, K., Foster, R., et al. 2012, *Society of Photo-Optical Instrumentation Engineers (SPIE) Conference Series*, Vol. 8453, *Characterization of the silicon drift detector for NICER instrument*, 845318
- Rau, A., Grotova, I., Gokus, A., et al. 2021, *The Astronomer's Telegram*, 14646, 1
- Remillard, R. A., Loewenstein, M., Steiner, J. F., et al. 2022, *AJ*, 163, 130
- Revnivtsev, M., Churazov, E., Gilfanov, M., & Sunyaev, R. 2001, *A&A*, 372, 138
- Roming, P. W. A., Kennedy, T. E., Mason, K. O., et al. 2005, *Space Sci. Rev.*, 120, 95
- Sasaki, M., Knies, J., Haberl, F., et al. 2022, *A&A*, 661, A37
- Scargle, J. D. 1982, *ApJ*, 263, 835
- Schlafly, E. F., Finkbeiner, D. P., Jurić, M., et al. 2012, *ApJ*, 756, 158
- Smale, A. P. & Kuulkers, E. 2000, *ApJ*, 528, 702
- Stellingwerf, R. F. 1978, *ApJ*, 224, 953
- Strohmayer, T. & Bildsten, L. 2006, *New views of thermonuclear bursts*, Vol. 39, 113–156
- Strüder, L., Briel, U., Dennerl, K., et al. 2001, *A&A*, 365, L18
- Sunyaev, R., Arefiev, V., Babyshkin, V., et al. 2021, *A&A*, 656, A132
- Swank, J. H., Becker, R. H., Boldt, E. A., et al. 1977, *ApJ*, 212, L73
- Treiber, H., Vasilopoulos, G., Bailyn, C. D., et al. 2021, *MNRAS*, 503, 6187
- Turner, M. J. L., Abbey, A., Arnaud, M., et al. 2001, *A&A*, 365, L27
- Valdes, F. 2021, *The DECam Community Pipeline Instrumental Signature Removal* (<https://legacy.noirlab.edu/noao/staff/fvaldes/Pipelines/Docs/PL206/>)
- VanderPlas, J. T. 2018, *ApJS*, 236, 16
- Vasilopoulos, G., Koliopanos, F., Haberl, F., et al. 2021, *ApJ*, 909, 50
- Verner, D. A., Ferland, G. J., Korista, K. T., & Yakovlev, D. G. 1996, *ApJ*, 465, 487
- Willingale, R., Starling, R. L. C., Beardmore, A. P., Tanvir, N. R., & O'Brien, P. T. 2013, *MNRAS*, 431, 394
- Wilms, J., Allen, A., & McCray, R. 2000, *ApJ*, 542, 914
- Worpel, H., Galloway, D. K., & Price, D. J. 2013, *ApJ*, 772, 94